American Society of Mechanical Engineers

Eliott   Guenat

First   *Last*

ASME Paper Title: Thin gas film isothermal condensation in aerodynamic bearings

Authors: Eliott Guenat, Jürg Schiffmann

ASME Journal Title: Journal of Tribology

*VOR (version of record)

Thin gas film isothermal condensation in aerodynamic bearings

Eliott Guenat
Ecole Polytechnique Fédérale de Lausanne
Laboratory for applied mechanical design
Maladière 71b, CP 526, CH-2002 Neuchâtel 2
Email : eliott.guenat@epfl.ch

Jürg Schiffmann
Ecole Polytechnique Fédérale de Lausanne
Laboratory for applied mechanical design
Maladière 71b, CP 526, CH-2002 Neuchâtel 2

ABSTRACT

High-speed small-scale turbomachinery for waste heat recovery and vapor compression cycles are typically supported on gas-lubricated bearings operating close to the saturation conditions of the lubricant. Under particular conditions, the gas film might locally reach the saturation pressure with potentially hazardous effects on the performance of the gas bearing. The present work introduces a model based on the Reynolds equation and the development of cavitation modeling in liquid-lubricated bearings for condensing gas bearings. The effect of condensation on load capacity and pressure and density profiles are investigated for two 1D bearing geometries (parabolic, Rayleigh step and wedge) and varying operating conditions. The results suggest that the load capacity is generally negatively affected if condensation occurs. An experimental setup consisting in a Rayleigh-step gas journal bearing with pressure taps to measure the local fluid film pressure is presented and operated first in air and then in R245fa in near-saturated conditions. The comparison between the evolution of the fluid film pressure under perfect gas and near saturation conditions clearly suggest the occurrence of condensation in the fluid film. These results are

corroborated by the very good agreement with the model prediction.

Roman symbols

A	Finite difference terms matrix (-)
a	Finite difference coefficient (-)
b	Finite difference coefficient (-)
c	Finite difference coefficient (-)
d	Finite difference terms vector (-)
g	Elrod's switch function (-)
h	Clearance (m)
h_0	Nominal clearance (m)
L	Bearing length (m)
P	Pressure (Pa)
R	Rotor radius (m)
t	Time (s)
U	Bearing linear speed (m s^{-1})
W	Load capacity (N)
W_r	Load capacity ratio (-)
x	Coordinate in the inertial frame (m)

Greek symbols

α	Relaxation coefficient (-)
β	Bulk modulus (Pa)
Δx	Space increment
θ	Circumferential coordinate
Λ	Compressibility number
μ	Viscosity (Pa s)
ρ	Density (kgm^{-3})
ω	Rotor angular velocity (rad s^{-1})

Superscripts

$-$	Non-dimensional

Subscripts

1	Pressure tap 1
2	Pressure tap 2
3	Pressure tap 3
4	Pressure tap 4
5	Pressure tap 5
a	Ambient condition
$cond$	Groove
i	i-th grid element
$non-cond$	Inner
o	Nominal
sat	Outer

Acronyms

JFO	Jakobson-Floberg-Olsson
MRBS	Motor-rotor-bearing system

1 INTRODUCTION

The recent surge of interest for refrigerant-lubricated bearings in turbomachinery applications, mostly for heat pumping [1] and waste heat recovery application [2, 3], implies the use of gas lubricant close to their saturation pressure. The present work investigates theoretically and experimentally the case where the saturation line is locally crossed in a self-acting gas bearing.

1.1 Nature of the issue

The literature has seen a regain of interest for process-gas supported bearings over the past two decades. In particular, turbomachinery operating in close-loop conditions gain from the use of self-acting gas bearings in terms of lifetime, simplicity and cleanliness. Applications include heat pumps and waste heat recovery, where the gas lubricating the bearing can be close to saturation conditions. Since the compression occurring in the fluid film is nearly isothermal, the gas in the bearing might cross the saturation line and condense. Experimental hints of such condensation were reported at the dawn of the gas bearing "golden age" [4–6] in externally-pressurized steam bearings. Unterberg and Ausman [7] proposed a model for condensing vapor lubrication based on the Reynolds equation. They noticed that the Poiseuille flow term must disappear in the two-phase flow under the isothermal compression hypothesis. However, their mathematical treatment of the remaining Couette flow term is not physically justified, as it neglects the transition of the Reynolds equation from an elliptical to a hyperbolical form. In parallel, the analogous problem of cavitation in liquid-lubricated bearings enjoyed a extensive development, notably with the the Jakobson-Floberg-Olsson (JFO) theory [8, 9]. It distinguishes the pressure-varying single phase zone and the isobaric two-phase zone. The Reynolds equation is elliptical in the former zone but becomes hyperbolic in the latter, requiring a special mathematical treatment. Elrod developed an algorithm based on finite difference predicting the film reformation of the cavitation zone succesfully [10]. Vijayaraghavan [11, 12] improved Elrod's algorithm and analyzed the analogy of the two-phase Reynolds equation with transonic flows [13]. However, these significant developments in cavitation were not adapted to the problem of condensation in gas bearings. Zuber and Dougherty [14] derived a Reynolds equation for condensing gases under non-equilibrium, with vapor source and sink terms. However, the method requires models from the nucleation theory

for these non-equilibrium terms, which were not explored by the authors. So far, no physics based model exists in the literature that is able to capture the condensation effect in thin film lubrication.

1.2 Goals and objectives

The present work aims to 1) propose an adaptation of Elrod's algorithm to condensating gas bearings under isothermal conditions, 2) investigate the effect of condensation on simple gas bearing geometries and 3) confront the model with original experimental data.

1.3 Scope of the Paper

Elrod's algorithm [10] is adapted for condensation in gas lubrication and applied to the 1D Reynolds equation. Solutions of the algorithm are computed using a finite difference method for two 1D slider bearings geometries. Effects of condensation on the density and pressure fields are investigated for different compressibility numbers and saturation density ratios. The effects of condensation on the static bearing load capacity is studied. A test rig is presented for the measurement of the fluid film pressure in a Rayleigh step journal bearing, using R245fa. Finally, the condensation model predictions are compared to the pressure field measurements.

2 THEORY

The 1D dimensionless Reynolds equation under the assumption of steady-state and isothermality [15] is recalled here:

$$-\partial_{\bar{x}}\left(\bar{\beta}\bar{h}^3\partial_{\bar{x}}\bar{\rho}\right) + \Lambda\partial_{\bar{x}}\left(\bar{\rho}\bar{h}\right) = 0 \tag{1}$$

with the following non-dimensionaliztion:

$$\bar{\rho} = \rho/\rho_a \quad \bar{\beta} = \beta/P_a = \rho\partial_\rho P/P_a \quad \bar{x} = x/L \quad \bar{h} = h/h_0 \quad \Lambda = \frac{6\mu U L}{P_a h_0^2} \tag{2}$$

β is the bulk modulus defined as $\beta = \rho \partial_\rho P$. Elrod's switch function g is introduced in the Poiseuille flow term such that

$$g = \begin{cases} 1, \bar{\rho} < \bar{\rho}_{sat} \\ 0, \bar{\rho} \geq \bar{\rho}_{sat} \end{cases} \tag{3}$$

$$-\partial_{\bar{x}} \left(g \bar{\beta} \bar{h}^3 \partial_{\bar{x}} \bar{\rho} \right) + \Lambda \partial_{\bar{x}} \left(\bar{\rho} \bar{h} \right) = 0 \tag{4}$$

The effect of the switch function is to make the Poiseuille term vanish in the regions where the saturation pressure is reached. Physically, β drops to 0 in saturation, since P reaches a constant value. However, it is numerically convenient to keep β non-zero with the help of the ideal gas assumption and to update the value of g. Under this assumption, $\bar{\beta}$ and $\overline{P}$ become:

$$\bar{\beta} = \frac{\rho \partial_\rho P}{P_a} = \frac{\rho r T_a}{P_a} = \overline{P} \tag{5}$$

$$\overline{P} = \begin{cases} \bar{\rho}, & \bar{\rho} < \bar{\rho}_{sat} \\ \bar{\rho}_{sat}, & \bar{\rho} \geq \bar{\rho}_{sat} \end{cases} \tag{6}$$

In the two-phase domain, only the Couette term of Equ. 1 remains:

$$\partial_{\bar{x}}(\bar{\rho} \bar{h}) = 0 \quad \text{Therefore} \quad \bar{\rho} \bar{h} = cst \tag{7}$$

The Reynolds equation locally switches from an elliptical form to an hyperbolic form [13], resulting in a strictly forward transmission of information in the two-phase film. The switch function g is also used to numerically represent this transition in the remaining Couette term. The discretization

follows the method of Vijayaraghavan [11] in order to have a central scheme in the single phase domain and a upwind difference scheme in the two-phase domain:

$$\partial_{\bar{x}}(\bar{\rho}\bar{h}) \approx \frac{a\bar{\rho}_{i+1}\bar{h}_{i+1} + b\bar{\rho}_i\bar{h}_i + c\bar{\rho}_{i-1}\bar{h}_{i-1}}{2\Delta\bar{x}} \tag{8}$$

With

$$a = \frac{g_{i+1} + g_i}{2} \quad b = 2 - \frac{g_{i+1} + 2g_i + g_{i-1}}{2} \quad c = -\left(2 - \frac{g_i - g_{i-1}}{2}\right) \tag{9}$$

If all three points $(i-1, i, i+1)$ are in single phase, then $a = 1$, $b = 0$ and $c = -1$, resulting in a centered difference scheme. If all three points are in the saturated zone, $a = 0$, $b = 2$ and $c = -2$, leading to an upwind difference scheme for the Couette term.

For the treatment of the Poiseuille term following Vijayaraghavan [11], we can write:

$$g\frac{\partial\bar{\rho}}{\partial\bar{x}} = \frac{\partial g(\bar{\rho} - \rho_{sat}/\rho_a)}{\partial\bar{x}} - (\bar{\rho} - \rho_{sat}/\rho_a)\frac{\partial g}{\partial\bar{x}} = \frac{\partial g(\bar{\rho} - \rho_{sat}/\rho_a)}{\partial\bar{x}} \tag{10}$$

because the spatial derivative of g is zero everywhere at the boundary, where $\rho = \rho_{sat}$. Therefore the Poiseuille term is expressed as follows:

$$-\partial_{\bar{x}}\left(\bar{\beta}\bar{h}^3 g\partial_{\bar{x}}\bar{\rho}\right) = -\partial_{\bar{x}}\left(\bar{\beta}\bar{h}^3\partial_{\bar{x}}\left(g(\bar{\rho} - \rho_{sat}/\rho_a)\right)\right) \tag{11}$$

$$= \frac{-1}{\Delta\bar{x}}\left(\bar{\beta}_{i+1/2}\bar{h}^3_{i+1/2}g_{i+1}(\bar{\rho}_{i+1} - \rho_{sat}/\rho_a)\right. \tag{12}$$

$$-(\bar{\beta}_{i+1/2}\bar{h}^3_{i+1/2} + \bar{\beta}_{i-1/2}\bar{h}^3_{i-1/2})g_i(\bar{\rho}_i - \rho_{sat}/\rho_a) \tag{13}$$

$$\left. +\bar{\beta}_{i-1/2}\bar{h}^3_{i-1/2}g_{i-1}(\bar{\rho}_{i-1} - \rho_{sat}/\rho_a)\right) \tag{14}$$

The resulting system of equation is expressed in the form :

$$A\vec{\rho} = \vec{d} \tag{15}$$

The non-linear equation is solved iteratively using the following scheme:

$$\vec{\rho}^n = (1 - \alpha)\vec{\rho}^{(n-1)} + \alpha A^{-1}\vec{d} \tag{16}$$

where $0 < \alpha \leq 1$ is a relaxation coefficient. The process is stopped when the following convergence coefficient is met :

$$\max_i \left| \frac{\rho_i^{(n)} - \rho_i^{(n-1)}}{\rho_i^{(n-1)}} \right| < 10^{-6} \tag{17}$$

3   NUMERICAL COMPUTATIONS AND RESULTS

The model is applied on different infinitely long bearing geometries as shown in Fig 1: a parabolic bearing (Case A) and a Rayleigh step bearing (Case B). All bearings have a ratio of 2 between the largest and the smallest clearance point. The boundary conditions of Eq. 4 are :

$$\bar{\rho} = 1 \text{ at } \bar{x} = 0 \text{ and } \bar{x} = 1 \tag{18}$$
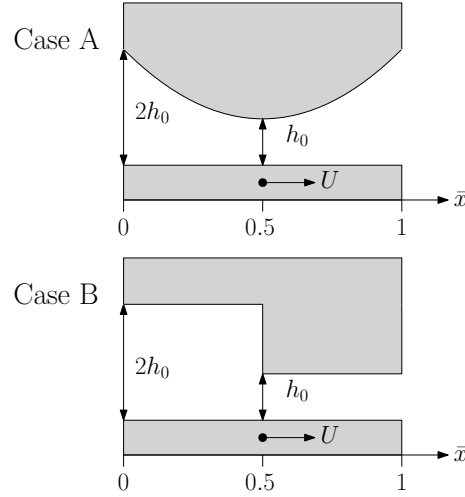
Fig. 1. Description of the two evaluated 1D bearing geometries: Parabolic and Rayleigh step

The clearance for the two layouts is expressed as follows:

$$\bar{h} = 4\bar{x}^2 - 4\bar{x} + 2 \qquad\qquad \text{Case A} \qquad\qquad (19)$$

$$\bar{h} = \begin{cases} 2, & \bar{x} < 0.5 \\ 1, & \bar{x} \geq 0.5 \end{cases} \qquad\qquad \text{Case B} \qquad\qquad (20)$$

The bearing model for a condensing lubricant is solved for different compressibility numbers Λ and saturation density $\bar{\rho}_{sat}$ in order to highlight the effects of condensation on the pressure and density fields: first varying $\bar{\rho}_{sat}$ at constant $\Lambda = 20$ (Fig 2 and 4) and then varying Λ at constant $\bar{\rho}_{sat}$ (Fig 3 and 5). The bearing domain is composed of 335 points, which achieves grid convergence, as presented in Fig. 6. The selected number of grid points leads to a relative error on two successive grid size on the load capacity of Case B of less than 0.1%, which is considered as acceptable in this context.

In all cases, the pressure and density lines are superposed in the single phase domain because of the ideal gas assumption. They diverge, however, in the two-phase flow domain, where the density follows the equation $\partial_{\bar{x}}(\bar{\rho}\bar{h}) = 0$ and the pressure remain bounded to the saturation pressure corresponding to the ambient temperature. The density increases by the formation of
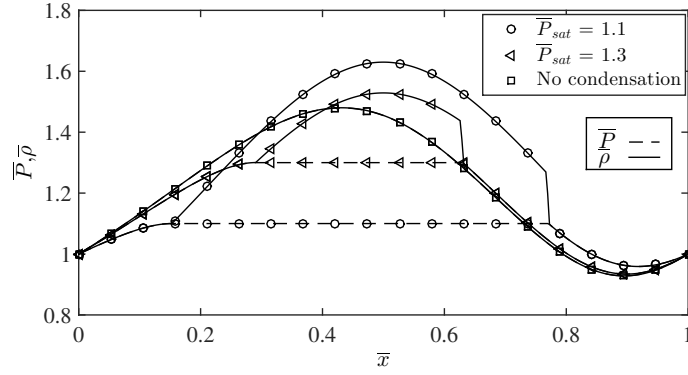
Fig. 2.   Pressure and density profiles in Case A for different saturation densities at $\Lambda = 20$
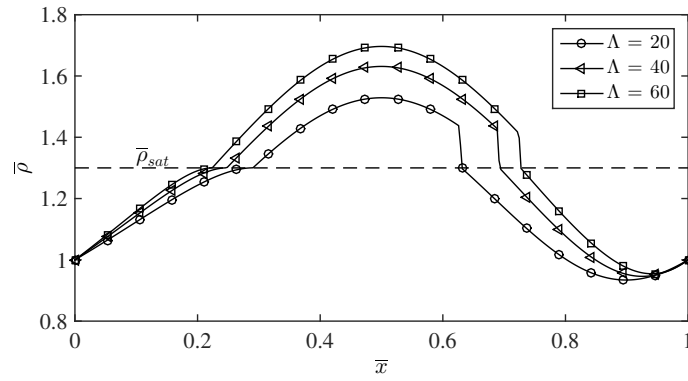
Fig. 3.   Density profiles in Case A for different compressibility numbers and $\bar{\rho}_{sat} = 1.3$
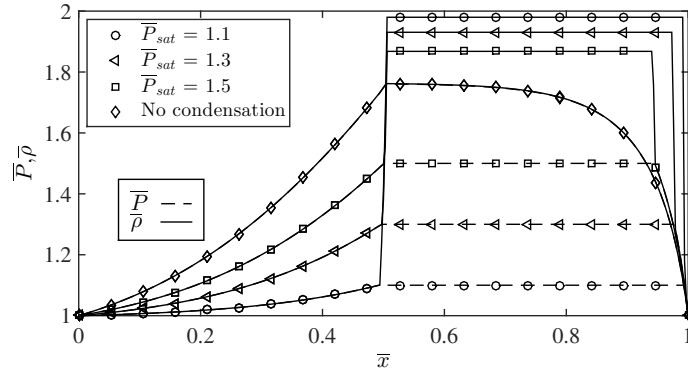
Fig. 4.   Pressure and density profiles in Case B for different saturation densities and $\Lambda = 20$

liquid in the fluid film, thus decreasing the vapor quality. The two-phase zone stops suddenly with a sharp density drop down to the saturation level. The effect of decreasing $\overline{P}_{sat}$ on the pressure and density field of Case A is represented in Fig. 2. At the point where the saturation pressure and density are reached, the Poiseuille flow must vanish in order to respect the mass continuity,

Guenat
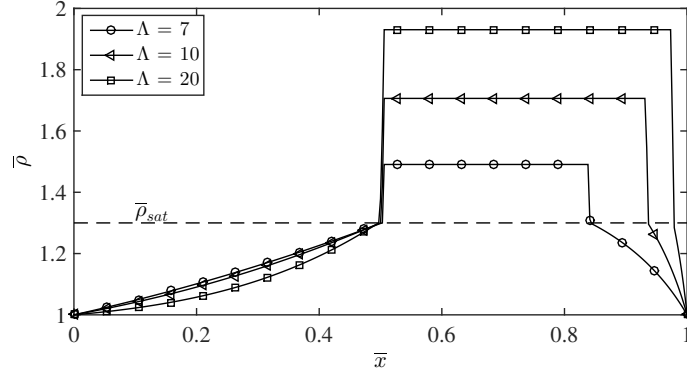
Fig. 5.   Density profiles in Case B for different compressibility numbers and $\bar{\rho}_{sat} = 1.3$
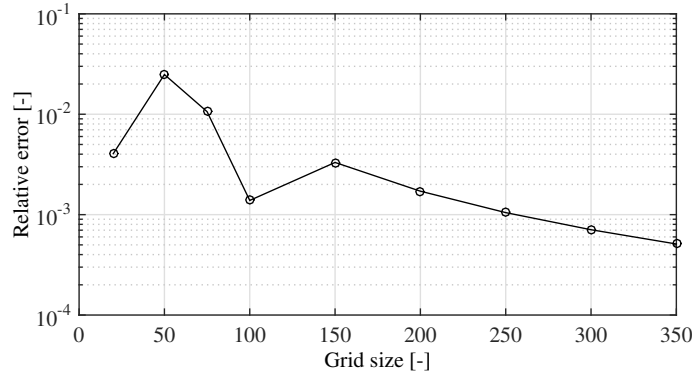
Fig. 6.   Relative error on the load capacity (Eq.21) between two successive grid sizes computing Case B at $\Lambda = 20$ and $\bar{P}_{sat} = 1.5$

resulting in a condition $\partial_{\bar{x}}\overline{P} = 0$ upstream of the condensing zone. As the saturation pressure decreases, the effect of condensation of the upstream single-phase flow increases, locally reducing the slope in the profiles. The onset of condensation occurs closer to the leading edge, while the maximum density in the two-phase zone is larger when the saturation pressure is lower. The sharp decrease of density, happening in the second half of the bearing, is postponed toward the trailing edge as $\overline{P}_{sat}$ decreases. However, following Eq. 7, the location of the maximum density is independent of the saturation pressure and corresponds to the point of minimum clearance. As far as Case A is concerned, an increase of compressibility number is qualitatively similar to a decrease of saturation pressure, as shown in Fig. 3. Increasing Λ leads to a spatially extended two-phase domain as well as a higher maximum density at the point of smallest clearance. The amplitude of the density drop at the end of the two-phase domain is not significantly affected by

the variation of compressibility number. Figure 4, representing the density and pressure fields of Case B for different saturation pressures, displays a different behavior. The saturation conditions are always met at the position of the step, independently of the saturation density $\overline{P}_{sat}$, as long as condensation is met in the density field. The discontinuity in the clearance allows the pressure derivative just upstream of the condensation onset to be non-zero, while respecting the mass flow conservation across the step. The density remains at a constant value in the two-phase domain, in accordance with Eq. 7. As the saturation pressure decreases, the density increases and the end of the saturated domain is shifted toward the trailing edge. The effect of compressibility number on the density field, shown in Fig. 5, are small upstream of the condensation onset, but significant downstream of it. Both the density plateau in saturation, the location of the density drop and the second single-phase domain depend significantly on the compressibility number. A higher value is associated with a larger density level in saturation and a postponed re-entry point in the single-phase regime, mechanically leading to a larger pressure between this point and the trailing edge of the bearing.

The limitation of the maximum achievable pressure due to the occurrence of local condensation affects the load capacity of the bearing. The load capacity is calculated as follows:

$$\overline{W} = \int_0^1 \overline{P} \mathrm{d}\bar{x} \tag{21}$$

In order to assess the effect of condensation the following load capacity ratio is defined:

$$W_r = \frac{\overline{W}_{cond}}{\overline{W}_{non-cond}} \tag{22}$$

The load capacity ratio W_r against the compressibility number Λ for different saturation densities is shown in Figures 7 and 8 for cases A and B respectively. In Fig. 8, the reduction in load capacity for Case B reaches values up to 90% at a relative saturation density of 1.1 and $\Lambda > 40$.

Interestingly, the load capacity can be modestly improved at low compressibility numbers and low relative saturation densities, with a calculated improvement of maximum 6%. This is due to a local increase in pressure right after the onset of condensation along the bearing, as represented in Fig. 9 for Case B at $\Lambda = 2$. The second-half of the bearing exhibits a large pressure excursion above the non-saturated level as the saturation pressure is increased, which leads to a net gain in load capacity. This behavior is further illustrated in Fig. 10, which displays the relative pressure at different locations along the bearing against the relative saturation pressure. The relative pressure first increases with $\overline{P}_{sat}$ at every reported location, before experiencing a correction to a lower, steady-state value as the fluid film exits the two-phase domain becomes entirely single phase. The correction begins first close to the trailing edge of the bearing and progresses toward the location the step at $\bar{x} = 0.5$. The amplitude of the correction decreases toward the step but occurs on a narrower range of relative saturated pressure, as the correction ends simultaneously over the entire bearing. This end of correction corresponds to the point where the saturation pressure reaches the maximum pressure built by the bearing in single-phase regime. The loss of load capacity of Case A, displayed in Fig. 7, is qualitatively similar to Case B. A loss of 80% of the load capacity is observed at low saturation density and high compressibility number, while a modest gain in load capacity is observed for $\bar{\rho} = 1.1$ only. At equal compressibility number and saturation density, the relative load capacity is higher for Case A than for Case B. The latter has a higher maximum pressure, which enhances the condensation effect and therefore leads to a more pronounced loss in load capacity.
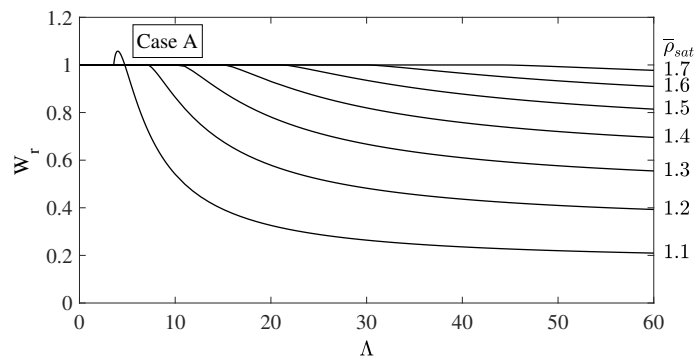
Fig. 7. Load capacity ratio in Case A for different saturation densities
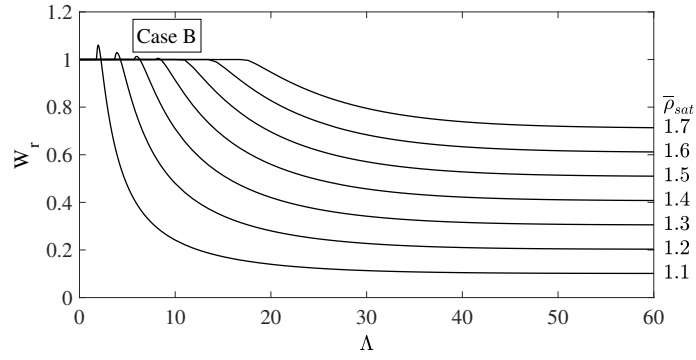
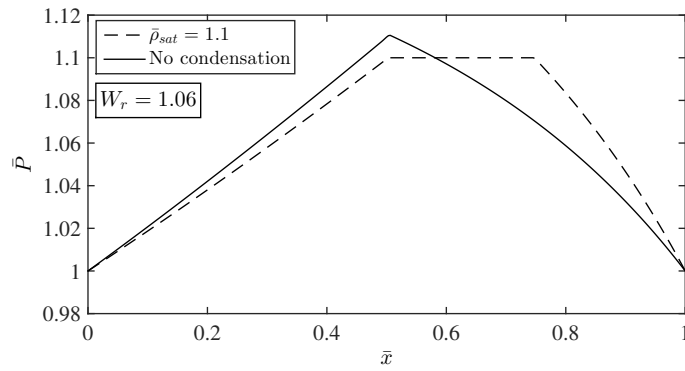Fig. 8.   Load capacity ratio in Case B for different saturation densities

Fig. 9.   Local increase in the pressure profile leading to a net gain in load capacity. Case B, $\Lambda = 2$
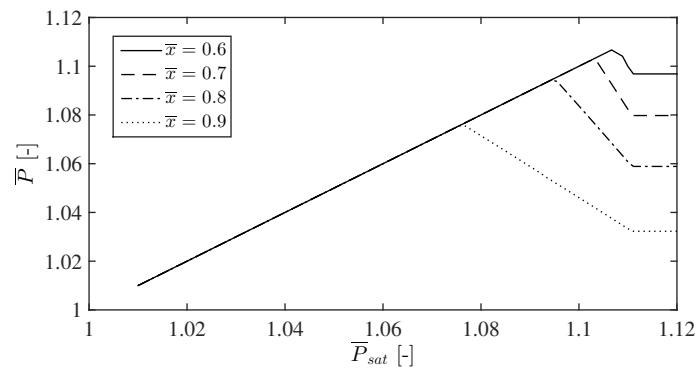

Fig. 10.   Evolution of the local pressure with the saturation pressure at 4 locations along the second half of a bearing (Case B, $\Lambda = 2$)

Guenat

4 EXPERIMENTAL SETUP AND RESULTS

To experimentally assess whether the isothermal condensation can occur in a gas bearing and to validate the theoretical model introduced above, an experimental setup is built. It consists of a 3-pocket Rayleigh step journal bearing driven by a flexibly coupled DC motor (Fig. 12). One of the bearing pocket is equipped with 5 pressure taps disposed along the circumferential direction at the mid axial span of the rotor (Fig. 13). A pocket is composed of a $5°$ wide 500 μm deep axial groove to establish the ambient pressure $\overline{P} = 1$, followed by a $30°$ wide region with a clearance of $16\mu m$ ($10 \pm 1\mu m$ step depth). The narrow region with a clearance of 6 ± 0.3 μm over $85°$ ends each of the three pads, as shown in Fig. 11. The rotor consists in a annular cylinder of with an outer diameter of 20 mm, an internal diameter of 6 mm with a length of 20 mm ($L/D = 1$). Both bearing and rotor are made of conventional steel. The maximal rotor speed of the electric drive is 60 krpm. The pressure taps consist of 10 mm long hollow tubes, with an outer diameter of 1.8 mm and an inner diameter of 200 μm. They are made of tungsten carbide and are press fitted into the bearing before the manufacturing of the grooves and the lapping of the inner diameter. The steps and grooves are manufactured with a 30 μm-diameter wire EDM process. As displayed in Fig. 13, the taps are located at 17°, 37°, 57°, 77° and 97° following the same circumferential reference as Fig. 11. The center of the second tap is located only $3°$ after the step in order to capture the point of maximum pressure.
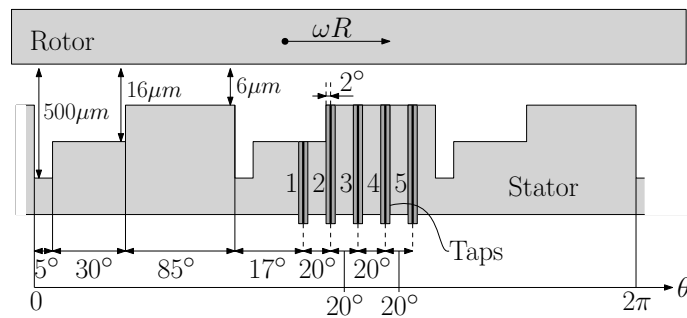
Fig. 11.   Geometry of the Rayleigh step journal bearing in the circumferential direction

The motor-rotor-bearing system (MRBS) is placed in vertical position in a pressure chamber. The vertical orientation unloads the rotor from the g-forces. A closed-loop cooling circuit feeds
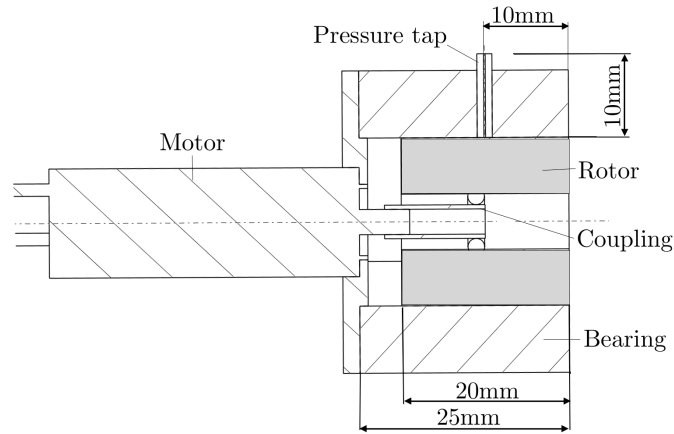
Fig. 12.   Axial cut of the motor-rotor-bearing system: 1) Motor 2) Bearing 3) Rotor 4) Coupling 5) Pressure tap
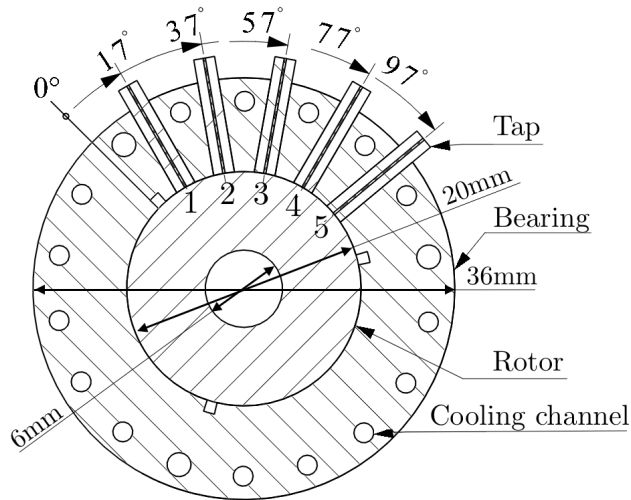

Fig. 13.   Cut of the motor-rotor-bearing system perpendicular to the rotor axis

water through the axial cooling channels of the bearing at a constant mass flow rate. A K-type, 0.28mm-diameter thermocouple with a precision of $\pm 0.5K$ is placed in the feed groove before the pocket equipped with pressure taps (Fig. 15). The water temperature in the cooling reservoir is measured using a high-precision reference PT100 thermometer with an uncertainty of $\pm 0.01K$. The speed is measured using the counter-electromotive force sensed by the motor controller. Pipes connect the 5 taps to a pressure scanner with an uncertainty of ± 0.002 bar at the pressure levels that will be considered. A sixth tube connected to the scanner measures the ambient

pressure in the chamber. In order to prevent undesired condensation in the measurement pipes, DC-fed coils heat the pressure measurement pipes in the chamber. The complete test apparatus is schematically presented in Fig. 14.
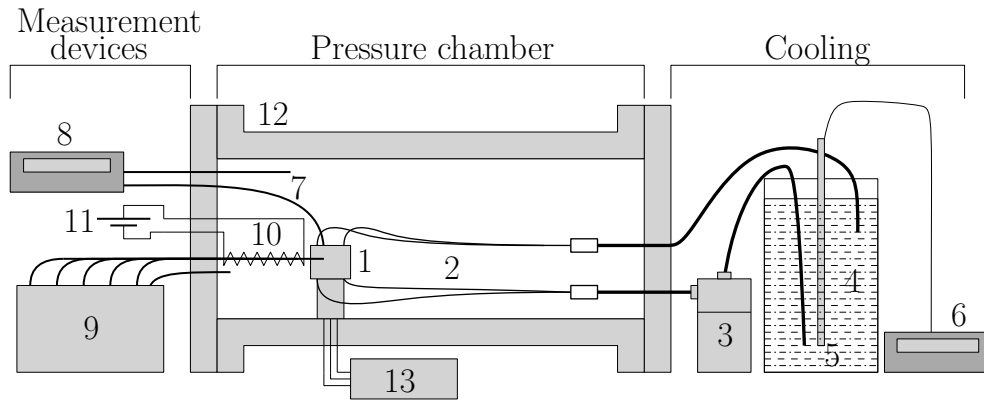
Fig. 14.   Test appartus: 1.MRBS 2.Cooling circuit 3.Circulation pump 4.Water reservoir 5.High-precision thermometer probe 6.Thermometer reader 7.Thermocouples 8.Thermocouple reader 9.Pressure scanner 10.Pressure pipe heater 11.DC source 12.Vessel 13.Motor drive
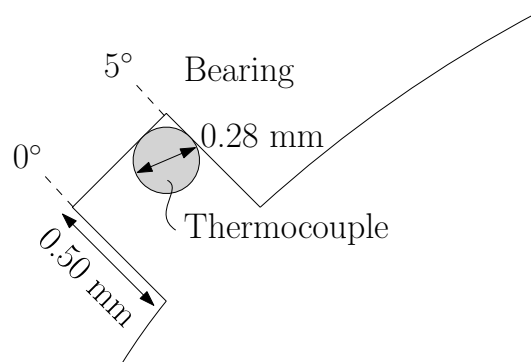
Fig. 15.   Location of the bearing thermocouple

4.1   Test runs in R245fa

The bearing is tested in an atmosphere of R245fa away from saturation conditions, in similar conditions as for the test runs in air. Fig. 16 shows the evolution of the 5 measured pressures accelerating from 3.6 to 30 krpm and coasting down to 0 rpm at t=125s. The pressure field at $t = 100s$ is compared to the predictions of the model in Fig. 17, taking into account the uncertainty

on the clearance and step depth in the modelling. Fluid parameters such as viscosity are computed with the help of the Coolprop database [16]. The model captures the pressure profile with a good agreement.
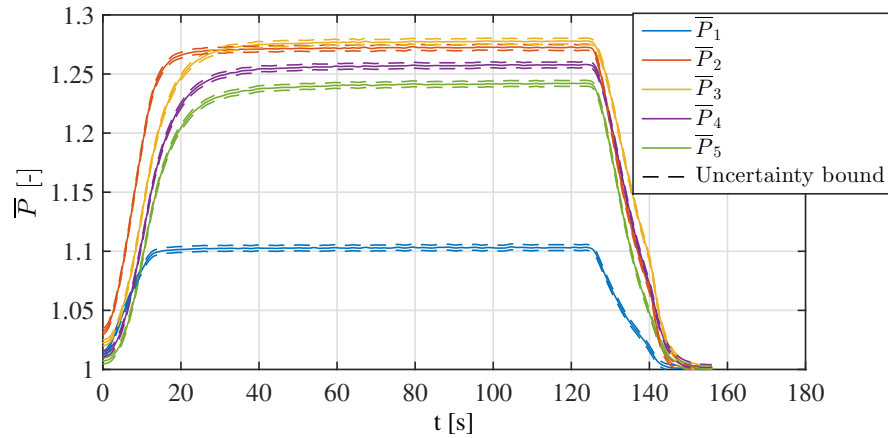
Fig. 16. Measured pressures against time in R245fa, $T_{bearing} = 23.4°$C $P_a = 96.0$ kPa, accelerating from 3.6 to 30 krpm

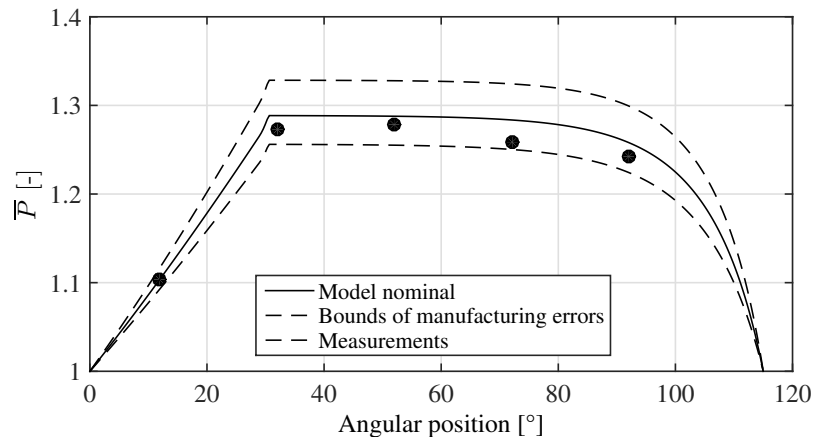Fig. 17. Comparison model-measurements in ambient air in non-saturated R245fa at 30 krpm, corresponding to $t = 100s$ in Fig. 16. Measurements uncertainty bounds are smaller that the diameter of the dots

The test procedure for condensation consist in pressurizing the pressure vessel at 1.18 bar with R245fa (corresponding saturation temperature is 19°C), a circulation of cooling water at 17°C in the bearing followed by a slow heating as the water warms up and the cooling capacity of the

circuit diminishes. When the cooling water at the pump intake reaches 21°C, which provides a 2K margin between the ambient and saturation pressures, the rotor is accelerated up to 30 krpm with a 10s ramp and kept at constant speed for several minutes, with the temperatures and pressures continuously measured. The evolution of the measured saturation pressure based on temperature measurements in the bearing and cooling water are displayed in Fig 18. Although its uncertainty is much lower, bounds of $\pm 0.1K$ on the measurements of the cooling water temperature are represented in order to grasp the influence of the temperature on the saturation pressure. Pressures P_2 to P_5 reach a nearly equal value from the start to $t \approx 300s$, and follow the trend of the temperature measured in the feed groove near the measurement point of P_1. As the bearing temperature rises, so does the pressure limit value, which corresponds to a saturation temperature 0.5 K higher than the measured bearing temperature. Compared to the test far from the saturation line (Fig. 16), this is a clear difference in the qualitative behavior, which can be considered a first hint for the occurrence of condensation in thin film lubrication. However, considering the cooling water temperature, the temperature in the capillaries has to be between the "hot" bearing surface and the "cold" cooling channels. Therefore, capillaries P_2 to P_5, are in saturated conditions and it cannot be excluded that condensation occurs within the measurement pipes, which may affect the value of pressure measured on the other side of the capillaries.

However, the observation of P_1 offers a more solid argument in favor of a condensing gas film: the saturation conditions are not met anywhere between the gas film and the pressure scanner, yet the measured pressure evolves with time beyond the settling time observed in Fig. 16 (≈ 12s), signaling a changing pressure in the gas film, in particular between 100 and 400s. This indicates that the pressure profile is influenced by the temperature as well as by the fluid film pressure downstream of the P_1, more than a simple change of viscosity (which increases by 1.4% over between 0 and 1000s).

In order to assess the effect of a pressure field perturbed at the location of the first pressure tap by the taps 2 to 5 acting as mass sinks due to the potential condensation in the capillaries, a test run in similar conditions as for Fig. 16 is repeated. This time, a manifold connecting the pressure taps to the ambient pressure is opened and the rotor is accelerated from 3.6 to 30krpm.

The taps 2 to 5 behave as gas sinks, since the pressurized gas can escape from the thin film to the ambient. After a couple of seconds, the manifold is closed, resulting in a pressure increase behind the taps 2 to 5 equalling the local pressure in the gas film. As shown in Fig 19 the closing of the manifold on taps 2-5 at t=35s, this results in a change of pressure measured at P_1. The change in pressure is $\Delta \overline{P} = 0.01$, which is significantly less than what is observed in Fig. 18, although the experiment with the manifold represents a pessimistic case scenario due to the large pressure difference across the taps. Therefore, the slowly rising P_1 is a consequence of the condensation within the fluid film at locations P_2-P_5.
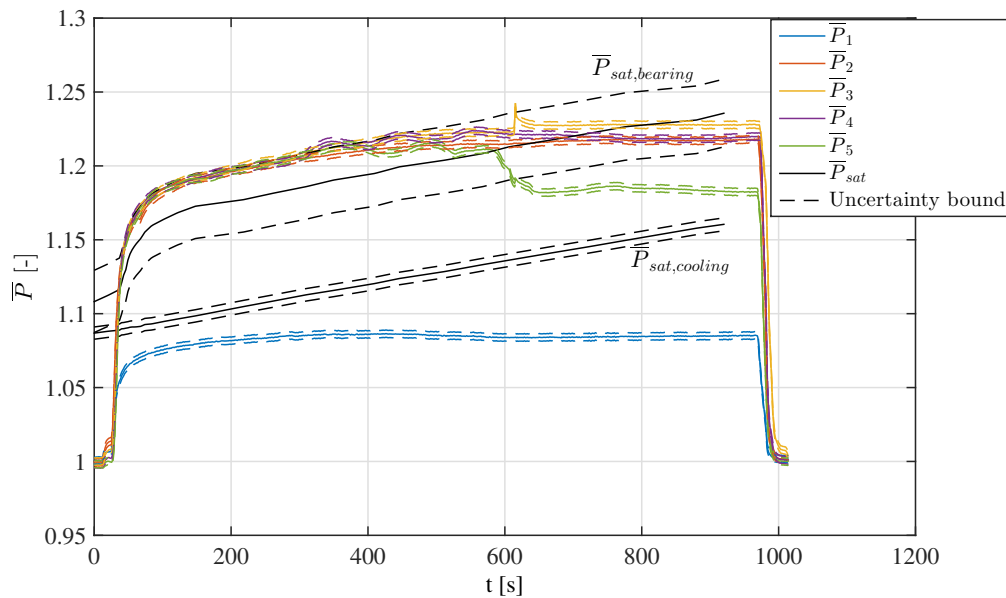
Fig. 18.   Measured pressures and computed saturation pressures against time

The condensation model is used to predict the pressure at the location of the pressure taps for a varying value of $\bar{\rho}_{sat}$ and compared to the measurements based on the measured bearing temperature. Since the saturation pressure based on the upper error band of the measured bearing temperature captures well the recorded pressure increases after the start, this value is used to calculate $\bar{\rho}_{sat}$ in the model. Comparisons are shown in Figures 20 and 21. Two interesting aspects are highlighted: first, the rising trend in P_1 experimentally observed appears in the simulations, al-
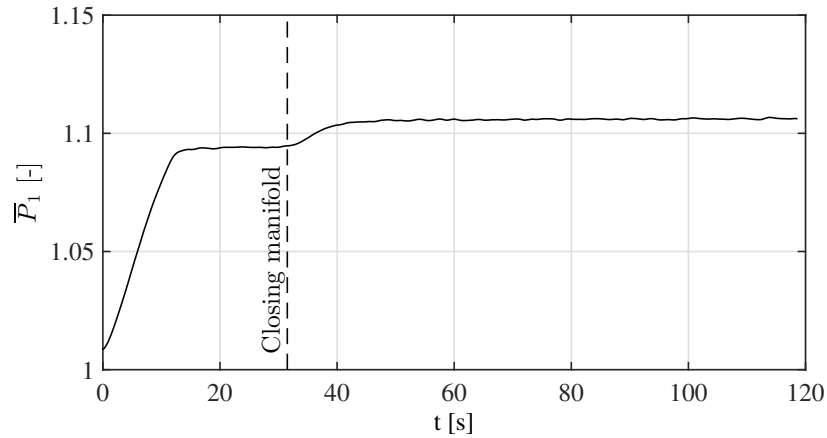
Fig. 19.   Influence of the opening and closing of the taps 2 to 5 on the pressure $\overline{P}_1$

though the predicted values are lower than the measured ones. Second, the sudden decrease of P_5 occurring around $t = 600s$ is predicted by the model. The sudden drop in pressure corresponds to the switch from the two-phase hyperbolic form of the Reynolds equation to the single phase, elliptical form, which is a consequence of the slowly rising temperature. The model also predicts a similar yet much smaller transition in P_4, which is not experimentally observed as clearly as for P_5. Some features appearing in the measurements, such as the oscillations in $\overline{P}_4$ and $\overline{P}_5$ between $t = 300s$ and $t = 600s$, are not captured by the model. They might be due to successive condensation and evaporation of liquid droplets in the pressure taps. Similarly, the sudden peak after $t = 600s$ in $\overline{P}_3$ is not captured by the model and can also be explained by the sudden evaporation of a metastable liquid droplet in the tap.

In a summary, the experimental campaign together with the the theoretical model clearly suggests the occurrence of condensation in a fluid film of a gas lubricated bearing operated close to the saturation line. The condensation is very sensitive to the local bearing temperature and the measurements seem to imply that condensing zones might appear and disappear, thus suggesting a dynamic behavior.

5   CONCLUSIONS

By applying the classical JFO cavitation theory and Elrod's numerical algorithm, a procedure for solving the Reynolds equation for a partially condensing gas is presented and solved for dif-
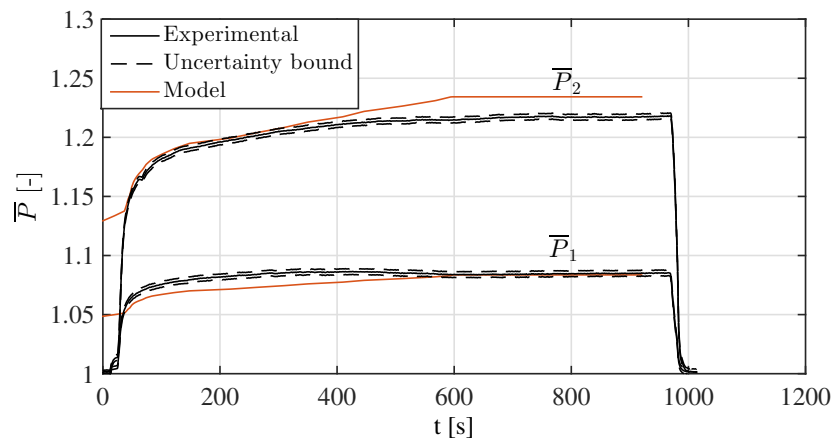
Fig. 20. Model-experimental comparison of $\overline{P}_1$ and $\overline{P}_2$ over time

ferent 1D slider bearing geometries. The effect of condensation on static pressure and density fields as well as load capacity is investigated for different compressibility numbers and saturation densities. Further, a test rig for the measurements of pressure in a Rayleigh step journal bearing is presented and used to compare the developed theory with experimental data. Both theoretical and experimental results suggest that:

   -The condensation greatly affects the pressure and density fields of a gas bearing by limiting the maximum pressure to the saturation pressure

   -The pressure level within the two-phase zone can be locally higher compared to the level it would reach without condensation

The theoretical results suggest that:

   -The load capacity is generally negatively affected by condensation in the gas film. However, exceptions with a increase in load capacity up to 6% are noted at low compressibility numbers

   -The phenomenon of isothermal condensation has been captured experimentally and is well predicted by the implemented 1D condensation model.

Further development of the presented theory would include a 2D implementation and its application to more widely employed bearing geometries such as spiral-grooved and foil bearings, both journal and thrust bearing configurations.
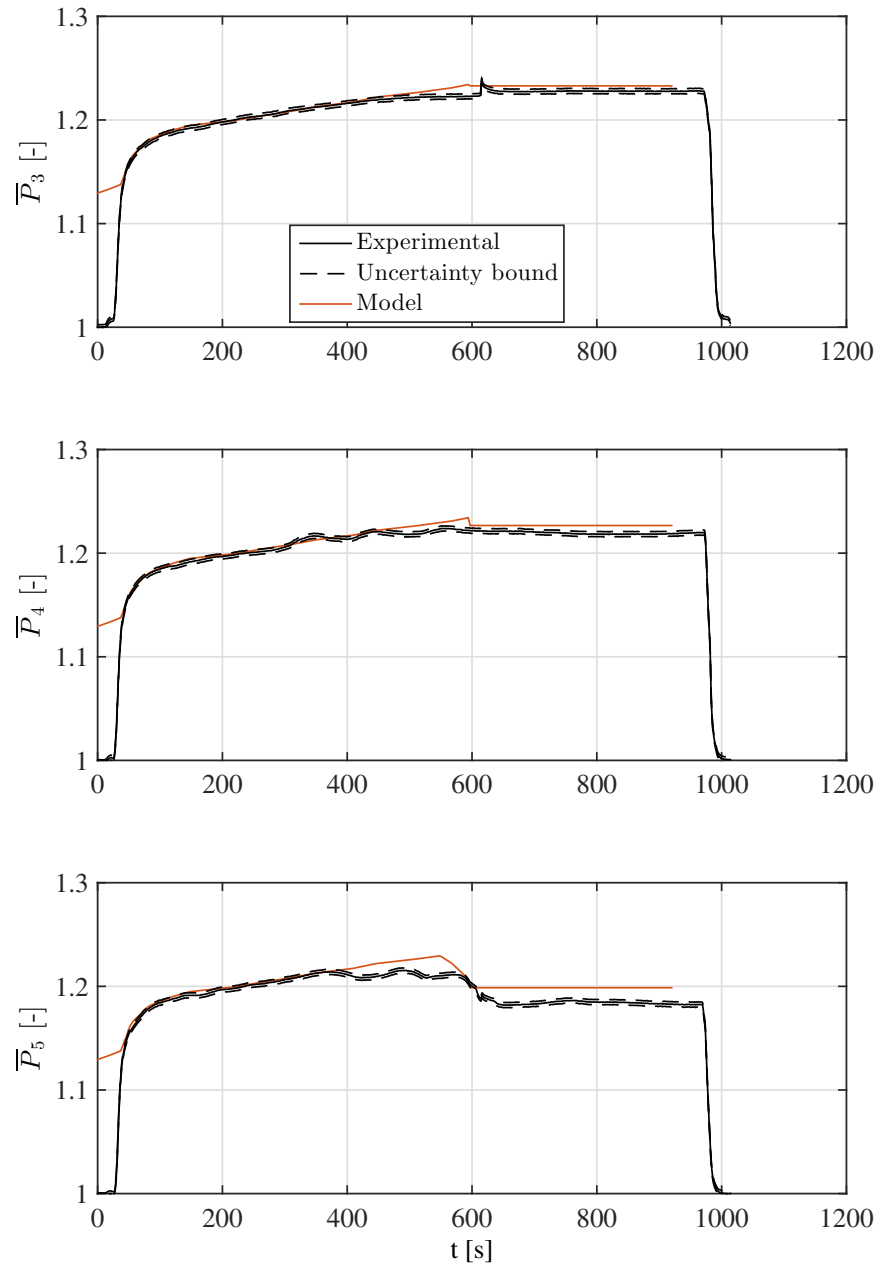
Fig. 21. Model-experimental comparison of $\overline{P}_3$, $\overline{P}_4$ and $\overline{P}_5$ over time

REFERENCES

[1] Javed, A., Arpagaus, C., Bertsch, S., and Schiffmann, J., 2016. "Small-scale turbocompressors for wide-range operation with large tip-clearances for a two-stage heat pump concept". *International Journal of Refrigeration,* **69**, pp. 285–302.

[2] Rosset, K., Mounier, V., Guenat, E., and Schiffmann, J., 2018. "Multi-objective optimization of turbo-ORC systems for waste heat recovery on passenger car engines". *Energy,* **159**, pp. 751–765.

[3] Mounier, V., Mendoza, L. C., and Schiffmann, J., 2017. "Thermo-economic optimization of an ORC driven heat pump based on small scale turbomachinery and comparison with absorption heat pumps". *International Journal of Refrigeration,* **81**, pp. 96–110.

[4] Elwell, R., 1961. "Observations on the performance of self- acting gas journal bearings. part II : Moisture condensation in self-acting gas bearings". *Technical Report, Contract No-2844(00) General Electric Laboratory*.

[5] Orcutt, F. K., 1963. "Experimental investigation of two-phase flow in thrust bearings". *Technical Report, Mechanical Engineering Incorporated,* **MTI-62TR40**.

[6] Orcutt, F. K., Dougherty, D. E., Malanoski, S. B., and Pan, C. H. T., 1968. "Investigation of externally pressurized steam-lubricated journal bearing". *Journal of Lubrication Technology,* **90**(4), pp. 723–730.

[7] Unterberg, W., and Ausman, J. S., 1966. "Condensing vapor lubrication of self-acting long journal bearings". *Journal of Basic Engineering*.

[8] Jakobsson, B., and Floberg, L., 1957. "The finite journal bearing considering vaporization". *Transactions of Chalmers University of Technology,* **190**, pp. 1–116.

[9] Olsson, K. O., 1965. "Cavitation in dynamically loaded bearings". *Transactions of Chalmers University of Technology,* **308**.

[10] Elrod, H. G., 1974. "A cavitation algorithm". *Mechanical Engineering Publications*, pp. 37–41.

[11] Vijayaraghavan, D., and Keith, T. G., 1989. "Development and evaluation of a cavitation algorithm". *Tribology Transactions,* **32**(2), pp. 225–233.

[12] Vijayaraghavan, D., and Keith, T. G., 1990. "Grid transformation and adaption techniques

applied in the analysis of cavitated journal bearings". *Journal of Tribology,* **112**(1), pp. 52–59.

[13] Vijayaraghavan, D., Keith, T. G., and Brewe, D. E., 1991. "Extension of transonic flow computational concepts in the analysis of cavitated bearings". *Journal of Tribology,* **113**, p. 539.

[14] Zuber, N., and Dougherty, D. E., 1982. "The field equations for two-phase reynolds film flow with a change of phase". *ASLE TRANSACTIONS,* **25**(1), pp. 108–116.

[15] Guenat, E., and Schiffmann, J., 2018. "Effects of humid air on aerodynamic journal bearings". *Tribology International,* **127**, pp. 333–340.

[16] Bell, I. H., Wronski, J., Quoilin, S., and Lemort, V., 2014. "Pure and pseudo-pure fluid thermophysical property evaluation and the open-source thermophysical property library CoolProp". *Industrial & Engineering Chemistry Research,* **53**(6), pp. 2498–2508.

LIST OF FIGURES